Deeply subwavelength metasurface resonators for terahertz wavefront manipulation

Mingkai Liu,[1,*] Quanlong Yang,[1,2] Ahmmed A. Rifat,[1] Vidur Raj,[3] Andrei Komar,[1] Jiaguang Han,[2] Mohsen Rahmani,[1] Haroldo T. Hattori,[4] Dragomir Neshev,[1] David A. Powell,[4] and Ilya V. Shadrivov[1]

[1] *Nonlinear Physics Centre, Research School of Physics and Engineering, Australian National University, Canberra ACT 2601, Australia*

[2] *Center for Terahertz Waves and College of Precision Instrument and Optoelectronics Engineering, Tianjin University, and the Key Laboratory of Optoelectronics Information and Technology Tianjin, Ministry of Education of China, Tianjin 300072, China*

[3] *Department of Electronic Materials Engineering, Research School of Physics and Engineering, Australian National University, Canberra ACT 2601, Australia*

[4] *School of Engineering and Information Technology, University of New South Wales, Canberra ACT 2610, Australia*

Metasurfaces offer a highly flexible platform for controlling the propagation and localization of electromagnetic waves. Due to the relatively large size of commonly used resonators, various undesirable effects including spatial dispersion and spurious diffraction occur, thus limiting the metasurface performance. To overcome these problems, one straightforward approach is to utilize deeply subwavlength meta-units. In contrast to conventional approaches that minimize the resonator size by reshaping the metallic patches, we reshape the capacitive gaps, an approach which is more robust to material loss, minimizing the problem of overdamping. As an example, we introduce a novel design based on interdigital capacitors (meander gap) with extremely subwavelength gaps for use in the terahertz frequency range. The size of our new resonator can be reduced to below $\lambda/30$ in a reflective-type terahertz metasurface, while maintaining the 2π phase shift required for full wavefront control. Using an advanced electron-beam lithography technique, we perform a proof-of-concept experiment and fabricate a 5mm $\times$ 5mm beam deflector, with the capacitive gaps as small as 300 nm ($\sim \lambda/1130$). The device performance is characterized using angle-resolved time-domain spectroscopy. Our study provides useful insight for ultra-compact metadevices based on deeply subwavelength meta-units working at terahertz frequencies and beyond.

KEYWORDS

metasurfaces, deeply subwavelength, terahertz, underdamped, wavefront

1. INTRODUCTION

Metasurfaces have shown tremendous capability to manipulate the propagation, scattering, polarization and localization of electromagnetic waves [1–4], extending previous studies of blazed gratings [5–7] and phased-array antennas [8, 9]. Typically, metasurfaces are discretized into many subwavelength resonant elements dubbed meta-atoms or meta-units [10, 11], each of which controls the local impedance as well as the amplitude and phase responses of the scattered wave. Although sparse discretization and large meta-units are favoured for ease of fabrication [12, 13], the influences of mutual interaction, spatial dispersion and discretization error also become prominent [14], and they need to be taken into account accurately during the design process [15], which can be very demanding for non-periodic metasurfaces. For challenging requirements including large metalenses with high numerical aperture, the required phase change becomes more and more dramatic as the lens diameter increases. As a result, the level of discretization, as is ultimately limited by the size of the meta-units, determines the maximal phase variation that can be approximated by the discretized metasurface without being undersampled, setting an upper limit on the achievable lens diameter for a given numerical aperture [16]. A recent study further showed that if evanescent modes are also involved, the number of meta-units required within each supercell can be significantly larger due to the smaller wavelength of evanescent modes, and highly subwavelength meta-units ($< \lambda/14$) are required to achieve the desired performance [17].

At low frequencies such as radio and microwave frequencies, resonators can be highly miniaturized due to the availability of reactive lumped elements, high index substrate materials, high conductivity metals, and the high resolution of lithography relative to the wavelength of operation [18–23]. However, at higher frequencies such as terahertz (THz) and infrared, reactive lumped elements are no longer available, and the miniaturization of meta-units typically relies on the novel design of distributed structures. The typical size of meta-units is of the order of $\lambda/5$ in most THz metasurfaces for wavefront control demonstrated to date [24, 25]. Deeply subwavelength resonators ($< \lambda/10$) have recently been demonstrated at THz frequencies, based on the concept of spoof localized surface plasmons [26–28], or a direct scaling down of the widely employed meanderline structures [29]. However, it remains unclear whether these concepts can be applied directly for efficient wavefront shaping, since

* mingkai.liu@anu.edu.au

the effect of over-damping in these deep-subwavelength resonators was not specifically examined.

In order to achieve efficient and arbitrary wavefront shaping, the metasurface needs to compensate for the phase difference between the incident field and the desired scattered field. This typically requires a resonant response, with which the transmission or reflection phase varies over the full 2π range. One strategy to realize a 2π phase shift is to spectrally overlap two resonant modes with opposite field parities. This concept has been applied to realize all-pass transmission filter based on photonic crystal slabs [30] and ultra-compact wave plates based on impedance-matched metamaterials [31, 32]. Recently, this concept was rejuvenated and generalized in the context of Huygens' metasurfaces and metadevices [33–37]. Another well-known meta-unit consists of a patch on top of a metallic ground plane, with a dielectric spacer in between [38–41]. To realize a 2π phase shift, it is essential that the resonant meta-units are under-damped, i.e. the radiative decay rate is greater than the nonradiative decay rate [42, 43]. This condition can be met by an appropriate design of the meta-unit, but it is challenging to make the meta-unit highly subwavelength while remaining under-damped [42], in particular at high frequencies where the conductivity of metal decreases [29, 44].

In this work, we demonstrate both theoretically and experimentally that reshaping the capacitive gaps between the metallic patches is the preferable approach to create deeply subwavelength meta-units. This strategy minimizes the problem of over-damping due to the poor conductivity of metals at high frequencies. This is in contrast to the strategy of reshaping the metallic patch into very thin and long shapes to increase the effective inductance, which readily leads to over-damping. Reshaping capacitive gaps is a practical route to shrink the meta-units below 1/25 of the operating wavelength, while remaining under-damped. Such deeply subwavelength meta-units provide more localized responses, minimizing the undesirable effects of mutual interaction, spatial dispersion and discretization error in metadevices.

2. RESULTS AND DISCUSSION

2.1. Two approaches for deep subwavelength meta-units

Each meta-unit support a series of resonances, and the impedance contribution of each resonance can be described by an effective RLC circuit. The simplest configuration of the patch is a rectangle (Figure 1a). To red-shift the resonance, there are two possible paths to reshape the meta-unit. The first path, which is widely applied, is to increase the effective inductance by reducing the width while increasing the total length of the metallic patch (Figure 1b); the second path is to increase the effective capacitance by reducing the separation while increasing the effective area of the gaps between metallic patches (Figure 1c).

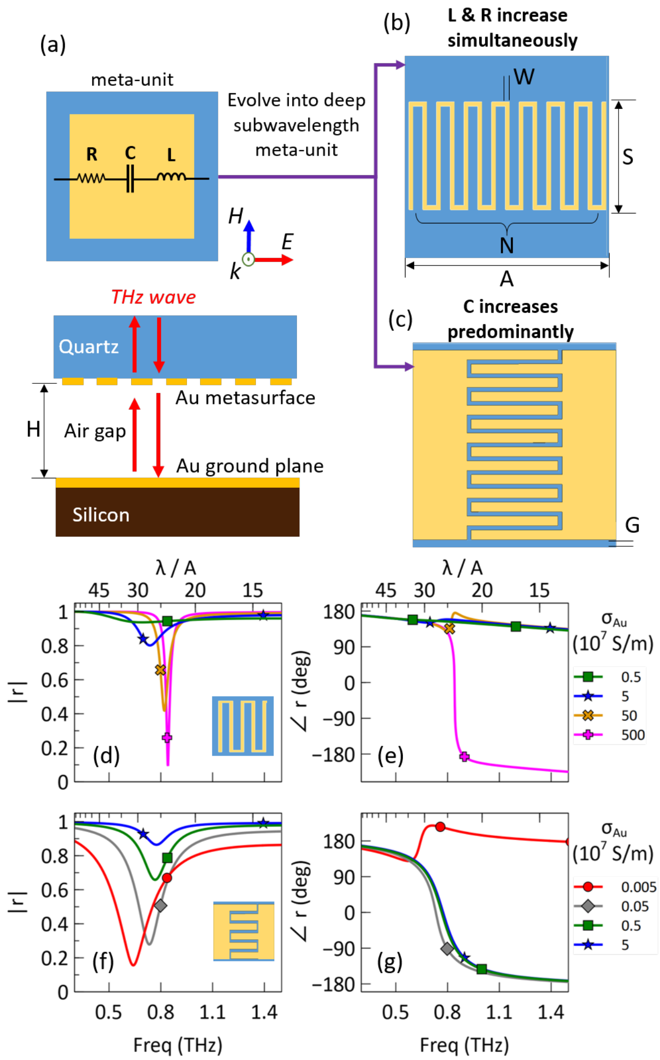

Figure 1. (a) Schematic of a reflective metasurface. The metallic patches can evolve into deep subwavelength meta-units by either (b) increasing the effective inductance L using a meander line or (c) increasing the effective capacitance C with a meander gap (interdigital capacitor). The simulated reflection (d) amplitude and (e) phase spectra of a metasurface with a meander line structure, for different values of the conductivity of gold. The corresponding responses of a metasurface based on the meander gap design are shown in (f) and (g). For the simulations from (d) to (g), we used the following geometries: A = 15 μm, W = 0.3 μm, H = 6 μm, G = 1 μm, S = 10 μm, and the number of interdigitated fingers N = 14. The thickness of the gold ground plane is 200 nm, and that of the patterned metallic layer is 100 nm.

Interestingly, the same type of shape transformation for the metallic patch to increase the effective inductance can also be applied to the dielectric gaps between patches to increase the effective capacitance. For example, the patch can be transformed into the well-known meander line to increase the inductance [18, 22, 23, 45], while the gap can also be transformed into a meander gap (also known as interdigital capacitor [46–48]). However, due to the strong Ohmic loss in the metal, the nonradiative decay rate quickly exceeds the radiative decay rate in the meander line, as it becomes longer and thinner. As a result, the resonance becomes over-damped and the 2π phase shift is destroyed when the resonance is red-shifted to a certain level. Our numerical study shows, that when the conductivity of metal is not high, the meander line design can not offer a significant size reduction without becoming over-damped. In contrast, the meander gap transformation is much more robust to material loss.

To show such a difference, we compare the responses of two metasurfaces based on the meander line and meander gap meta-units for different values of conductivity of gold σ_{Au} (Figure 1d to 1g). Note that to mimic the conditions in our subsequent experimental demonstration, the THz wave is incident from and reflected back to a quartz environment (permittivity around 4.4) in the simulation. Both designs of meta-units have the same lattice constant A, number of fingers N, width W, finger length S, as well as height H of the air gap (for detailed geometries, see caption of Figure 1). The parameters are chosen such that the size of meta-units is around 1/25 of the resonant wavelength when $\sigma_{Au} = 5\times10^7$ S/m, which is much more subwavelength than conventional designs. For the meander line design, the resonance is severely over-damped when a realistic level of conductivity σ_{Au} is applied (in the order of 5×10^6 to 5×10^7 S/m [49]). Even when the conductivity is increased by 3 orders of magnitude, the resonance remains close to critically damped (near perfect absorption) due to the intrinsically low radiative decay rate (Figure 1e). In contrast, the 2π phase shift remains achievable in the meander gap design even when the conductivity is set to one order of magnitude below the realistic level (Figure 1g). This is because the radiative decay rate in this structure is much higher than the one of meander line structure, as can be inferred from the difference in the linewidths of the resonances.

2.2. Equivalent circuit model

To have a more in-depth understanding of why the meander line approach is more sensitive to material loss, we extract the resonant frequency ω_0 as well as the radiative and nonradiative decay rates Γ_{rad} and Γ_{abs} by fitting the simulated complex reflection coefficients around the resonance to the following model based on single Lorentzian resonance [50]:

$$r = e^{(-i\beta-\alpha)\omega H/c}\left[-1 + \frac{i2\omega\Gamma_{rad}}{\omega_0^2 - \omega^2 + i\omega(\Gamma_{rad}+\Gamma_{abs})}\right], \tag{1}$$

where additional parameters β and α are introduced as the effective propagation and decay constants, in order to have a better match with the nonresonant background

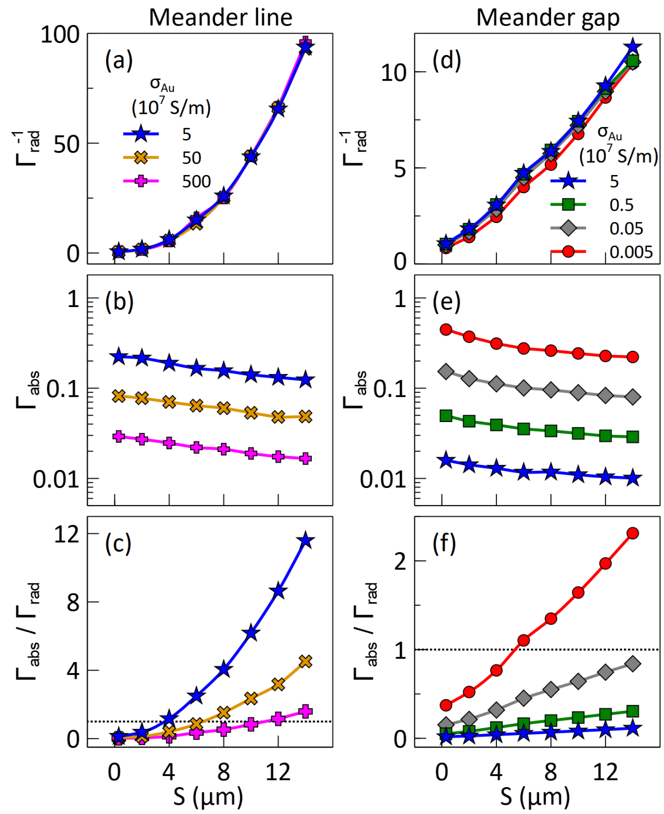

Figure 2. The change of radiative decay rate Γ_{rad} and nonradiative decay rate Γ_{abs} as a function of the finger length S, for different values of conductivity. (a) to (c) Meander line structure, (d) to (f) Meander gap structure. All geometric parameters other than S are identical to those used in Figure 1d to 1g.

continuum. These two parameters change gradually as S increases, and they are different for meander line and meander gap structures. Compared to the simplified model based on coupled mode theory [42], our model also works well for low-Q resonances and ensures that $|r| \to 1$ when $\omega \to 0$. The two decay rates Γ_{rad} and Γ_{abs} are plotted in Figure 2 as functions of the finger length S, for different values of the conductivity of gold.

For both meander line and meander gap designs, Γ_{rad} and Γ_{abs} decrease as the finger length S increases (see Figure 2a,b and d,e). Under the same conductivity $\sigma_{Au} = 5\times10^7$ S/m, meander line structures have a smaller Γ_{rad} and a larger Γ_{abs} than the meander gap structure. The most important difference is that Γ_{rad} follows a different scaling rule in the two structures: $1/\Gamma_{rad} \propto \mathrm{S}^2$ in meander lines while $1/\Gamma_{rad} \propto$ S in meander gaps (see Figure 2a and 2d). This difference eventually leads to a drastic different behavior of the ratio $\Gamma_{abs}/\Gamma_{rad}$, which grows in a quadratic-like fashion in meander line structures, but almost linearly in meander gap structures (Figure 2c and 2f). The dotted lines in Figure 2c and 2f mark $\Gamma_{abs}/\Gamma_{rad} = 1$, which is the phase transition point between the under-damped state ($\Gamma_{abs}/\Gamma_{rad} < 1$) and the over-damped state ($\Gamma_{abs}/\Gamma_{rad} > 1$). It is clear that in meander line structures, the resonance becomes over-damped much faster with increasing S.

To understand this intriguing behavior, we employ a circuit model (see Figure 3). The model starts with a transmission line that has an impedance of the incident environment (semi-infinite quartz superstrate), then a series RLC circuit (top metasurface) connected with a short transmission line that represents the air gap, ending with a short circuit (ground plane) [51]. The resonant frequency is given by $\omega_0 = 1/\sqrt{LC}$ and the linewidth $\Gamma_{abs} = R_{abs}/L$, where the effective circuit parameters take into account the interaction between the top metasurface and the ground plane. Simulations show that for both meander line and meander gap structures, the resonant frequency decreases approximately as 1/S, i.e. $\omega_0 \propto 1/\mathrm{S}$, while Γ_{abs} only shows a slow decrease (Figure 2b and 2e). These features indicate the approximate linear scaling rule of the effective circuit parameters: $L \approx L_0 + a_L\mathrm{S}$ and $C \approx C_0 + a_C\mathrm{S}$ such that $\omega_0 \propto 1/\mathrm{S}$, and $R_{abs} \approx R_0 + a_R\mathrm{S}$ such that Γ_{abs} only shows a slow change with S. a_L, a_C and a_R are constant coefficients that describe the variation of L, C and R as linear functions of S. The change of the effective inductance L and the non-radiative resistance R_{abs} is more prominent in meander lines, while the change of the effective capacitance C is the major contribution in meander gaps. These approximate relations are consistent with the geometric dependency of the effective circuit parameters in monolithic meander line inductors and interdigital capacitors [52], and the first order approximation is valid when the size of the element is highly subwavelength.

Meanwhile, Γ_{rad} decreases rapidly, following approximately a $1/\mathrm{S}^2$ relation in the meander line structure but an approximate 1/S relation in the meander gap structure, as shown in Figure 2a and 2d. For excitation at normal incidence, the input surface impedance of the meta-unit Z_i can be expressed as

$$Z_i = \frac{Z_d Z_s}{Z_d + Z_s}, \tag{2}$$

where

$$Z_s = i\omega L_s + 1/(i\omega C_s) + R_s \tag{3}$$

is the effective impedance of the top layer of the metasurface. Assuming the nonradiative loss is only contributed by the top layer of the metasurface, we have $R_s = R_{abs}$.

$$Z_d = \frac{i\eta}{\sqrt{\epsilon_2}}\tan(kH\sqrt{\epsilon_2}) \approx \frac{i\eta\omega H}{c} = i\omega L_d \tag{4}$$

is the effective impedance of the optically-thin dielectric layer on the ground plane, which acts as an effective inductor $L_d = \eta H/c$. $\eta = \sqrt{\mu_0/\epsilon_0}$ is the wave impedance of vacuum, and ϵ_2 is the permittivity of the dielectric layer (in our case $\epsilon_2 = 1$, $kH \approx 0.1$).

Since we are interested in the radiative decay rate, for simplicity, we neglect the nonradiative loss ($R_s = 0$ such that $\Gamma_{abs} = 0$). Then the input impedance Z_i can be expressed as

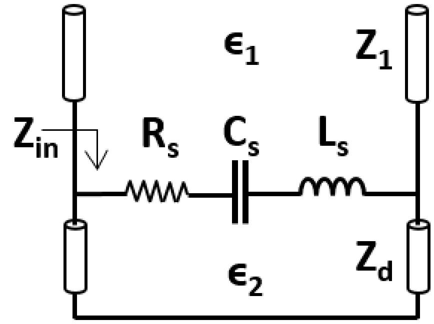

Figure 3. Schematic of the transmission line model of the metasurface.

$$\begin{aligned} Z_i &= \frac{[i\omega L_s + 1/(i\omega C_s)](i\omega L_d)}{i\omega(L_s + L_d) + 1/(i\omega C_s)} \\ &= \frac{i\zeta\omega(-\omega^2 L_s + 1/C_s)}{\omega_0^2 - \omega^2}, \end{aligned} \tag{5}$$

where $\omega_0 = 1/\sqrt{(L_s + L_d)C_s}$ is the resonant frequency and $\zeta = L_d/(L_s + L_d)$ is the ratio of the effective inductance of the thin dielectric layer to the total effective inductance of the meta-unit.

The reflection coefficient of the meta-unit can be calculated from the impedance mismatch

$$r = \frac{Z_i - Z_1}{Z_i + Z_1}, \tag{6}$$

$Z_1 = \eta/\sqrt{\epsilon_1}$ is the impedance of the incident environment (in out case $\epsilon_1 = 4.4$). Substituting Equation (5) into Equation (6), we have

$$\begin{aligned} r &= \frac{i\zeta\omega(1/C_s - \omega^2 L_s)/Z_1 - (\omega_0^2 - \omega^2)}{i\zeta\omega(1/C_s - \omega^2 L_s)/Z_1 + (\omega_0^2 - \omega^2)} \\ &= -1 + \frac{i2\omega\zeta(1/C_s - \omega^2 L_s)/Z_1}{\omega_0^2 - \omega^2 + i\omega\zeta(1/C_s - \omega^2 L_s)/Z_1} \end{aligned} \tag{7}$$

If we compare Equation (7) with the bracket part of Equation (1) (assuming $\Gamma_{abs} = 0$), it is clear that

$$\Gamma_{rad} = \frac{\zeta}{Z_1}\left(\frac{1}{C_s} - \omega^2 L_s\right) \tag{8}$$

At the resonant frequency, $\omega = \omega_0 = 1/\sqrt{(L_d + L_s)C_s}$, the relation between the radiative decay rate and the effective reactive parameters is given by:

$$\Gamma_{rad} = \frac{L_d^2}{Z_1}\frac{1}{(L_d + L_s)^2 C_s} \propto \frac{1}{L^2 C}, \tag{9}$$

where we denote $C = C_s$ and $L = L_d + L_s$ as the effective circuit parameters of the meta-unit, as shown in Figure 1a. Since L_d only depends on the thickness of the dielectric layer H, the change of L with respect to the finger length S is contributed by L_s.

Equation (9) indicates that when tailoring geometry to reduce the radiative decay rate, increasing the effective inductance is much more beneficial than increasing the effective capacitance. This feature explains the different scaling rules of Γ_{rad} observed for the meander line and meander gap structures in Figure 2. Therefore, to create deeply subwavelength meta-units which are not over-damped, it is preferable to increase the effective capacitance while minimizing the change of the effective inductance and non-radiative resistance. Increasing the finger overlap in the meander gap structure follows this desired trend, making it an attractive implementation of deeply subwavelength meta-units.

2.3. Design of beam deflector using meander gap meta-units

Due to its ability to remain under-damped, the meander gap design is a practical platform to achieve deeply subwavelength meta-units with a full phase control of the reflection coefficient. To demonstrate this, we simulate the reflection coefficients for different finger lengths S while keeping other parameters unchanged (Figure 4a and b). To take into account various loss mechanisms such as the finite thickness of the gold film, the surface roughness and the grain boundary effect [49, 53], we use a conductivity $\sigma_{Au} = 5 \times 10^6$ S/m, around one order of magnitude lower than the values typically found in the literature. As the finger length S increases from 0.3 μm (i.e. a simple rectangular patch) to 14 μm, the resonant frequency red-shifts dramatically, and the ratio of the resonant wavelength to the lattice constant A becomes larger than 30 (Figure 4a and 4b). We use H = 6 μm to match the experimental condition. The resonant wavelength can be further pushed to around 40A when H is increased from 6 μm to 10 μm.

To test if such resonators can be applied to wavefront shaping, we design a metasurface beam deflector composed of a periodic array of supercells; each of which consists of spatially varying meta-units with different finger lengths S (Figure 4c). The metasurface works for TE polarized waves, and the beam deflection angle in the quartz is designed to be around 13 degrees at 0.88 THz. The corresponding length of the supercell is 690 μm, with 46 meta-units. The designed finger lengths S increase monotonically across the supercell, as shown in Figure 4c, and they are chosen, such that the local reflection phase varies linearly from $-180°$ to $180°$ at 0.88 THz (Figure 4d). At this frequency, the size of the unit A $\approx \lambda/23$, and the capacitive gap W $\approx \lambda/1136$. Note that the 13° diffraction angle in quartz corresponds to around 30° in air, which will be confirmed in experiment. With the 690 μm supercell size, there are five propagating Floquet modes allowed in air (i.e. the diffraction orders $-2, -1, 0, 1,$ and 2), and the efficiency of the diffraction order -1 is the one we aim to maximize with the linear blazed grating phase profile [54]. Simulation of the diffraction coefficients r_n of different orders shows that the optimal working frequency shifts slightly to around 0.9 THz (see Figure 4e), at which around 68% of the reflected wave energy is scattered into the diffraction order -1, 29% is lost as absorption and the remaining 3% is scattered into other diffraction orders. The wave deflection performance is further confirmed by the far-field scattering pattern, where spurious diffraction and specular reflection are negligible (Figure 4f). The electric field distribution shown in Figure 4g is the full-wave simulation of the time-averaged distribution of the superimposed incident and reflected fields, while the one shown in Figure 4h is the analytical result of two superimposed plane waves that represent the incident and the diffraction fields of order -1. A very good agreement between the two is shown.

One of the advantages of more subwavelength meta-units is that their responses are more localized and the effect of mutual interaction is smaller [15], minimizing spatial dispersion. In addition, the smaller unit size also indicates that the neighbouring meta-units are geometrically more similar in a spatially varying array, such that the simulation with periodic boundaries can provide a much better estimate of the mutual coupling. Although there is a slight change of the optimal operation frequency in our design due to the change of mutual interaction, the effect on the overall phase profile across the supercell is minor. Since the diffraction order -1 remains dominant, while specular reflection and spurious diffraction are strongly suppressed, the phase response across the supercell remains well matched to the designed linear function shown in Figure 4c. In the Supporting Information, we further demonstrate the performance of beam-deflectors designed for different beam-steering angles at 0.88 THz. Remarkably, simulations show that even at a large steering angle of 60°, the optimal operating frequency is barely shifted, and the diffraction efficiency of the order -1 is still as high as 63% (see Supporting Information). This is in stark contrast to metasurfaces with larger unit-cell size, which generally require global optimization of all geometric parameters for each designed diffraction angle. In the design of metasurfaces with sparse discretization, mutual interaction and spatial dispersion can have significant impacts and need to be taken into account [15].

2.4. Experimental confirmation

To further demonstrate the feasibility of a meander gap metasurface, we fabricated a beam deflector sample (around 5 mm × 5 mm) using electron-beam lithography (EBL) (Figure 5b). The challenge of such fabrication is achieving nanoscale gap size (300 nm) across a centimeter-scale area. Photo-lithography, which is the conventional method for fabricating THz metasurfaces, is not applicable for such nano-fabrication. Therefore, to

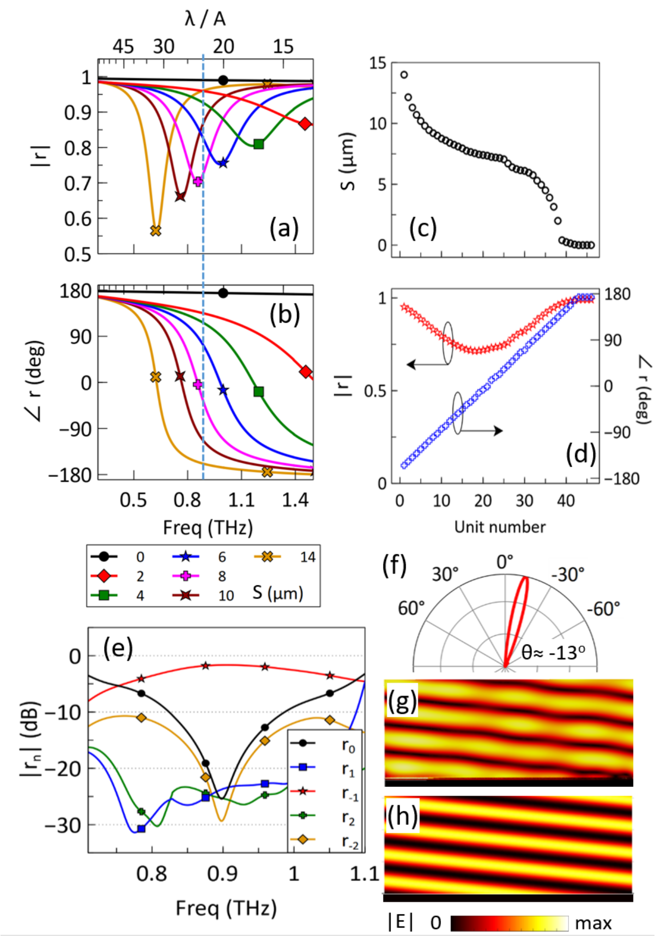

Figure 4. (a) and (b) Simulated reflection coefficients of a meander gap metasurface as a function of the finger length S. Except where specified, parameters are identical to those used in Figure 1f and g. The conductivity $\sigma_{Au} = 5 \times 10^6$ S/m. (c) The chosen finger lengths over a supercell of a metasurface beam deflector and (d) the corresponding local reflection coefficients at 0.88 THz. (e) The amplitude of reflection into each diffraction order supported by the metasurface. (f) Simulated farfield scattering pattern in quartz and (g) the time-averaged interference pattern of the incident and reflected electric fields. (h) Analytical result of the time-averaged interference pattern of two plane waves, with one propagating at normal incidence and the other propagating at the angle of the diffraction order -1 ($\theta \approx -13°$).

fabricate the beam deflector sample, we developed a new recipe, with optimised doses and step-sizes, via 30 kV EBL (Raith 150). First, 3 nm Cr was evaporated as an adhesion layer, onto a 1 mm thick quartz substrate, followed by 100 nm Au evaporation. Subsequently, 500 nm positive tone ZEP electro-resist was spin coated on the sample, followed by EBL patterning. After developing the resist, the patterns were transferred to the Au film via ion milling. Finally, the resist was washed away. In parallel, another silicon substrate was covered by 200 nm Au, to act as a ground plane mirror. The scanning electron microscope (SEM) images confirm that the meander gap size is indeed around 300 nm (Figure 5d and 5e). To create an air gap, plastic balls with nominal dimensions 5 μm to 6 μm, commonly used as spacers in liquid crystal displays, were evenly distributed on the un-patterned regions of the metallic film (Figure 5a). The metasurface sample was then covered with the ground plane substrate, and the two samples were bonded to each other using ultraviolet curing glue "Norland Optical Adhesive 60".

The performance of the sample was measured using angle-resolved THz time-domain spectroscopy [55]. As shown in Figure 6a, a pair of fiber-based terahertz antennas were employed as the transmitter and receiver. The antennas were mounted on the guide rails and the rotator controlled the incident and detection angles of the terahertz wave. The incident terahertz wave was collimated by a lens before illuminating the sample. The sample was positioned at the center of the rotator and illuminated by the transmitter at normal incidence. The reflected signals were picked up by the receiver at different angles θ. In order to minimize the spectral fringes due to the Fabry-Perot effect from the quartz substrate, the measured time-domain signals were time-gated before being Fourier-transformed into the frequency-domain.

The measured angle-resolved spectra are plotted in Figure 6b, and they are normalized to the specular reflection spectrum from a mirror, which was measured at 10 degrees. As shown by the dashed curve in Figure 6b, the peaks of the measured reflection amplitudes have a good match with the angles of the diffraction order -1, predicted by the grating formula: $\theta_{-1} = -\arcsin(\lambda/P)$, where P $=$ 690 μm is the size of the supercell lattice. Note that the measured angle of diffraction is not around $-13°$ but around $-30°$, due to refraction at the interface between quartz and air (Figure 6d). We further confirm that the reflected wave is predominantly diffracted in a single direction, as the signals picked up in the opposite angle direction $-\theta$ are at the noise level. However, the measured maximal amplitude of reflection into the desired order is around 0.3, accounting for around 9% of the incident energy. The measured peak diffraction coefficients under different angles θ from Figure 6b are re-plotted in Figure 6c as $|r_{-1,exp}|$.

To understand the energy loss, we measured the zeroth order reflection amplitude $|r_{0,exp}|$ from the sample, which is more than 0.65 (Figure 6c), meaning that more than 42% of the energy is reflected specularly. The remaining 50% is lost due to absorption and spurious diffraction. The simulated and measured spectra are shown in Figure 6c for comparison. Despite the discrepancy between the measured and the simulated coefficients due to the unexpectedly large specular reflection, the overall trend of the measured spectra shows a good qualitative match with the simulation. The increased specular reflection and reduced diffraction efficiency in the measured spectra could be attributed to several factors. The first is that the conductivity of the deposited gold layer could

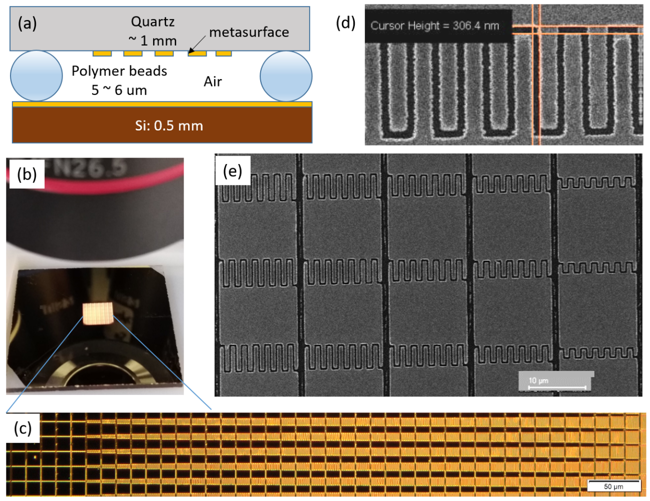

Figure 5. (a) Schematic of the metasurface sample. (b) Photograph, (c) dark-field microscopy image, (d) and (e) scanning electron microscope (SEM) images of the fabricated sample.

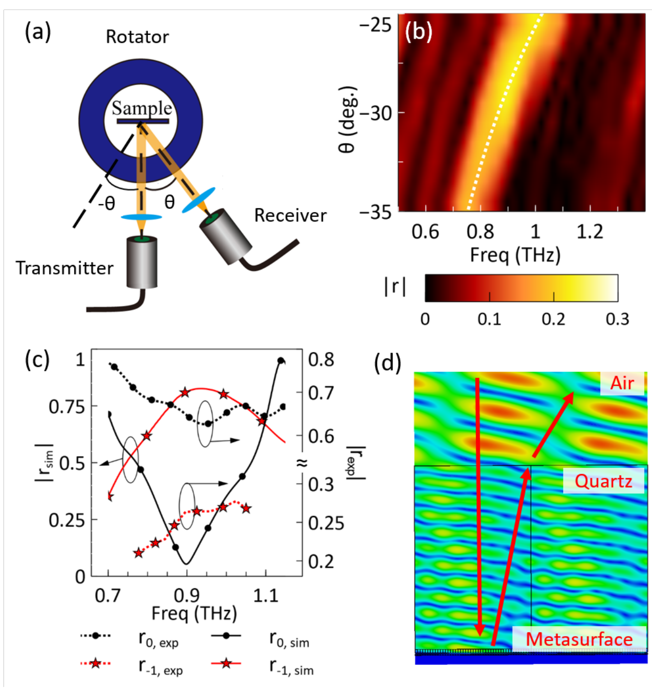

Figure 6. (a) Schematic of the fiber-based THz time-domain spectroscopy system for the angle-resolved reflection spectra measurement. (b) The measured angle-resolved reflection spectra. The white dashed curve indicates the angles of the diffraction order -1 calculated by theory. (c) Measured and simulated diffraction spectra of the sample. (d) Simulated time-averaged field distribution of the sample with a 1 mm thick quartz substrate.

be even lower than the simulated one ($\sigma_{Au} = 5 \times 10^6$ S/m), even though it is already one order of magnitude lower than the conventional one quoted in the literature. The conductivity reduction due to grain boundaries and surface roughness could be more noticeable due to the nanometer scale gap size. The second reason is the finite thickness of the quartz superstrate, around 12.5% of the energy is reflected at the air/quartz interface when the Fabry-Perot effect is not taken into account (as we have filtered it by time-gating the time-domain signals). The third reason is the non-uniformity of the air gap thickness. The fourth reason is the finite incident beam width that effectively introduces components at oblique incidence. The fifth possible cause could be the residual of the gold and chromium within a small part of the capacitive nano-gaps, leading to an increase of the specular reflection. While further study and examination are required to understand the difference between the simulation and experiment, the measured result confirms that the fabricated metasurface functions as a beam deflector and that tailoring the capacitive gap is a practical strategy for constructing deeply subwavelength meta-units for metasurface devices.

3. CONCLUSION

To conclude, we have introduced a practical route to realize deeply subwavelength meta-units in reflective metasurfaces for terahertz wavefront control. Combining numerical simulation and a circuit model, we found that instead of reshaping the metallic patches to red-shift the resonance, it is more advantageous to tailor the capacitive gaps, as this minimizes the problem of over-damping. We compared the performance of terahertz metasurfaces based on meander lines and meander gaps, and found that the latter are much more robust against material loss. Based on the meander gap structure, we designed and fabricated a terahertz metasurface beam deflector with highly subwavelength unit-cells ($\sim \lambda/23$) and capacitive gaps ($\sim \lambda/1136$), using advanced electron beam lithography. The designed beam steering was confirmed with the measurement using terahertz time-domain spectroscopy. Since the dielectric spacer in our design is air, it allows a direct hybridization with various platforms based on micro-electromechanical systems (MEMS) to achieve dynamical tuning of the reflection phase by changing the size of the air gap [56–59]. The application of deeply subwavelength meta-units provides a straightforward approach to mitigate the undesirable effects due to sparse discretization, including spatial dispersion, mutual interaction and discretization error. We expect that this study will provide useful insight and new possibilities for the development of ultra-compact metadevices working at high frequencies.

AUTHOR CONTRIBUTION

M. Liu conceived the idea, performed the theoretical and numerical studies. A. Rifat, V. Raj, A. Komar, M. Rahmani fabricated the sample. Q. Yang measured the sample under the supervision of J. Han. D. A. Powell, H. T. Hattori, D. Neshev and I. V. Shadrivov supervised the project. M. Liu wrote the manuscript, with input from all coauthors.

ACKNOWLEDGEMENTS

This work was supported by the Asian Office of Aerospace Research and Development (AOARD) (FA2386-15-1-4064), the Linkage grant LP160100253. M. Liu thanks Andreas Olk for the valuable comments and discussion.

CONFLICT OF INTEREST

The authors declare no conflict of interest.

SUPPORTING MATERIALS: BEAM DEFLECTORS FOR DIFFERENT STEERING ANGLES

To show the advantage of deeply subwavelength meta-units, we design and simulate the performance of beam deflectors that steer a normally incident beam towards different diffraction angles. The results are summarized in Figure 7. The optimal operation frequencies for different designed steering angles change slightly around 0.88 THz (between 0.86 and 0.9 THz), but the overall diffraction efficiency of the order -1 remains largely unchanged. Even at 60 degrees of beam steering angle, the diffraction efficiency of the order -1 is still as high as 63%, while the specular reflection and spurious diffractions remain well suppressed.

[1] S. B. Glybovski, S. A. Tretyakov, P. A. Belov, Y. S. Kivshar, C. R. Simovski, *Phys. Rep.* **2016**, *634*, 1.
[2] P. Genevet, F. Capasso, F. Aieta, M. Khorasaninejad, R. Devlin, *Optica* **2017**, *4*, 139.
[3] F. Ding, A. Pors, S. I. Bozhevolnyi, *Rep. Prog. Phys.* **2017**, *81*, 026401.
[4] D. Neshev, I. Aharonovich, *Light: Sci. Appl.* **2018**, *7*, 58.
[5] T. Aoyagi, Y. Aoyagi, S. Namba, *Appl. Phys. Lett.* **1976**, *29*, 303.
[6] P. Lalanne, S. Astilean, P. Chavel, E. Cambril, H. Launois, *J. Opt. Soc. Am. A* **1999**, *16*, 1143.
[7] J. Feng, Z. Zhou, *Opt. Lett.* **2007**, *32*, 1662.
[8] D. Berry, R. Malech, W. Kennedy, *IEEE Trans. Antennas Propag.* **1963**, *11*, 645.
[9] D. Pozar, T. Metzler, *Electron. Lett.* **1993**, *29*, 657.
[10] N. Yu, F. Capasso, *Nat. Mater.* **2014**, *13*, 139.
[11] N. Meinzer, W. L. Barnes, I. R. Hooper, *Nat. Photonics* **2014**, *8*, 889.
[12] Y. Ra'di, D. L. Sounas, A. Alu, *Phys. Rev. Lett.* **2017**, *119*, 067404.
[13] A. M. Wong, G. V. Eleftheriades, *Phys. Rev. X* **2018**, *8*, 011036.
[14] M. A. Cole, A. Lamprianidis, I. V. Shadrivov, D. A. Powell, *arXiv:1812.04725* **2018**.
[15] A. E. Olk, D. A. Powell, *Phys. Rev. Appl.* **2019**, *11*, 064007.
[16] A. She, S. Zhang, S. Shian, D. R. Clarke, F. Capasso, *Opt. Express* **2018**, *26*, 1573.
[17] X. Wang, A. Díaz-Rubio, V. S. Asadchy, G. Ptitcyn, A. A. Generalov, J. Ala-Laurinaho, S. A. Tretyakov, *Phys. Rev. Lett.* **2018**, *121*, 256802.
[18] G. Marrocco, *IEEE Antennas Wirel. Prop. Lett.* **2003**, *2*, 302.
[19] J. Baena, L. Jelinek, R. Marques, J. Zehentner, *Appl. Phys. Lett.* **2006**, *88*, 134108.
[20] P. Jin, R. W. Ziolkowski, *IEEE Antennas Wirel. Prop. Lett.* **2010**, *9*, 501.
[21] M. Beruete, M. Navarro-Cía, V. Torres, M. Sorolla, *Phys. Rev. B* **2011**, *84*, 075140.
[22] P. Kolb, T. Salter, J. McGee, H. Drew, W. Padilla, *J. Appl. Phys.* **2011**, *110*, 054906.
[23] W.-C. Chen, C. M. Bingham, K. M. Mak, N. W. Caira, W. J. Padilla, *Phys. Rev. B* **2012**, *85*, 201104.
[24] T. Niu, W. Withayachumnankul, B. S.-Y. Ung, H. Menekse, M. Bhaskaran, S. Sriram, C. Fumeaux, *Opt. Express* **2013**, *21*, 2875.
[25] I. Al-Naib, W. Withayachumnankul, *J. Infrared, Millimeter, Terahertz Waves* **2017**, *38*, 1067.

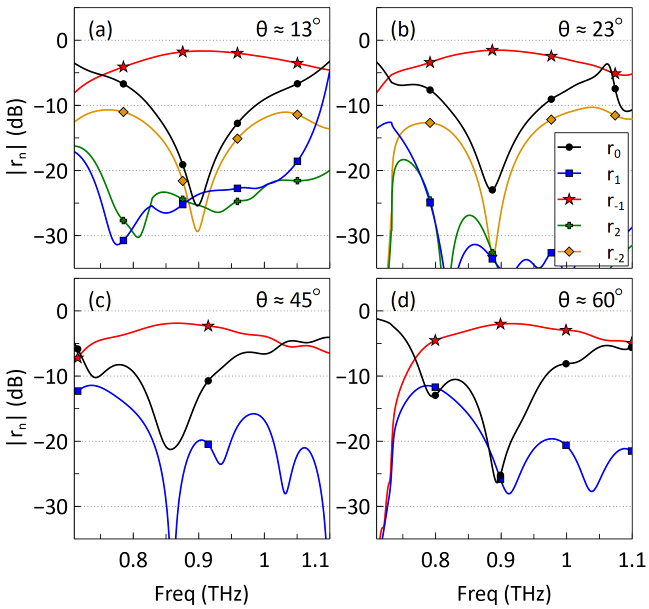

Figure 7. (a) to (d) Simulated diffraction coefficients of metasurface beam deflectors designed for different beam steering angles at 0.88 THz.

[26] A. Pors, E. Moreno, L. Martin-Moreno, J. B. Pendry, F. J. Garcia-Vidal, *Phys. Rev. Lett.* **2012**, *108*, 223905.
[27] P. A. Huidobro, X. Shen, J. Cuerda, E. Moreno, L. Martin-Moreno, F. Garcia-Vidal, T. J. Cui, J. Pendry, *Phys. Rev. X* **2014**, *4*, 021003.
[28] Z. Gao, L. Wu, F. Gao, Y. Luo, B. Zhang, *Adv. Mater.* **2018**, *30*, 1706683.
[29] Y. Chen, H. Zhou, X. Tan, S. Jiang, A. Yang, J. Li, M. Hou, Q. Guo, S.-w. Wang, F. Liu, H. Liu, F. Yi, *IEEE Photonics J.* **2018**, *10*, 1.
[30] W. Suh, S. Fan, *Appl. Phys. Lett.* **2004**, *84*, 4905.
[31] M. Liu, Y. Zhang, X. Wang, C. Jin, *Opt. Express* **2010**, *18*, 11990.
[32] P. Weis, O. Paul, C. Imhof, R. Beigang, M. Rahm, *Appl. Phys. Lett.* **2009**, *95*, 171104.
[33] C. Pfeiffer, A. Grbic, *Phys. Rev. Lett.* **2013**, *110*, 197401.
[34] M. Decker, I. Staude, M. Falkner, J. Dominguez, D. N. Neshev, I. Brener, T. Pertsch, Y. S. Kivshar, *Adv. Opt. Mater.* **2015**, *3*, 813.
[35] Y. F. Yu, A. Y. Zhu, R. Paniagua-Domínguez, Y. H. Fu, B. Luk'yanchuk, A. I. Kuznetsov, *Laser Photonics Rev.* **2015**, *9*, 412.
[36] A. Epstein, G. V. Eleftheriades, *J. Opt. Soc. Am. B* **2016**, *33*, A31.
[37] M. Liu, D.-Y. Choi, *Nano Lett.* **2018**, *18*, 8062.
[38] D. M. Pozar, S. D. Targonski, H. Syrigos, *IEEE Trans. Antennas Prop.* **1997**, *45*, 287.
[39] A. Pors, M. G. Nielsen, R. L. Eriksen, S. I. Bozhevolnyi, *Nano Lett.* **2013**, *13*, 829.
[40] G. Zheng, H. Mühlenbernd, M. Kenney, G. Li, T. Zentgraf, S. Zhang, *Nat. Nanotechnol.* **2015**, *10*, 308.
[41] S. Yu, L. Li, G. Shi, C. Zhu, X. Zhou, Y. Shi, *Appl. Phys. Lett.* **2016**, *108*, 121903.
[42] C. Qu, S. Ma, J. Hao, M. Qiu, X. Li, S. Xiao, Z. Miao, N. Dai, Q. He, S. Sun, L. Zhou, *Phys. Rev. Lett.* **2015**, *115*, 235503.
[43] Z. Miao, Q. Wu, X. Li, Q. He, K. Ding, Z. An, Y. Zhang, L. Zhou, *Phys. Rev. X* **2015**, *5*, 041027.
[44] L. Cong, P. Pitchappa, C. Lee, R. Singh, *Adv. Mater.* **2017**, *29*, 1700733.
[45] H. Wong, K.-M. Luk, C. H. Chan, Q. Xue, K. K. So, H. W. Lai, *Proc. IEEE* **2012**, *100*, 2109.
[46] G. D. Alley, *IEEE Trans. Microwave Theory Tech.* **1970**, *18*, 1028.
[47] A. Lai, T. Itoh, C. Caloz, *IEEE Microwave Mag.* **2004**, *5*, 34.
[48] W. Withayachumnankul, C. Fumeaux, D. Abbott, *Opt. Express* **2010**, *18*, 25912.
[49] N. Laman, D. Grischkowsky, *Appl. Phys. Lett.* **2008**, *93*, 051105.
[50] R. Alaee, M. Albooyeh, C. Rockstuhl, *J. Phys. D: Appl. Phys.* **2017**, *50*.
[51] F. Costa, S. Genovesi, A. Monorchio, G. Manara, *IEEE Trans. Antennas Propag.* **2013**, *61*, 1201.
[52] I. J. Bahl, *Lumped elements for RF and microwave circuits* Artech house**2003**.
[53] Q. G. Zhang, B. Y. Cao, X. Zhang, M. Fujii, K. Takahashi, *Phys. Rev. B* **2006**, *74*, 134109.
[54] S. Larouche, D. R. Smith, *Opt. lett.* **2012**, *37*, 2391.
[55] Q. Yang, X. Chen, Q. Xu, C. Tian, Y. Xu, L. Cong, X. Zhang, Y. Li, C. Zhang, X. Zhang, J. Han, W. Zhang, *Photonics Res.* **2018**, *6*, 1056.
[56] X. Liu, W. J. Padilla, *Adv. Opt. Mater.* **2013**, *1*, 559.
[57] Z. Han, K. Kohno, H. Fujita, K. Hirakawa, H. Toshiyoshi, *Opt. Express* **2014**, *22*, 21326.
[58] M. Liu, M. Susli, D. Silva, G. Putrino, H. Kala, S. Fan, M. Cole, L. Faraone, V. P. Wallace, W. J. Padilla, D. A. Powell, I. V. Shadrivov, M. Mariusz, *Microsyst. Nanoeng.* **2017**, *3*, 17033.
[59] X. Zhao, K. Fan, J. Zhang, G. R. Keiser, G. Duan, R. D. Averitt, X. Zhang, *Microsyst. Nanoeng.* **2016**, *2*, 16025.